Electrochimica Acta 542 (2025) 147431

Contents lists available at ScienceDirect

Electrochimica Acta

journal homepage: www.journals.elsevier.com/electrochimica-acta

Dependence of microstructure and mechanical properties of electrodeposited copper foils on electrochemical behavior of sodium saccharin

Che Liu [a,b], Zhao Cheng [b,*], Linhai Liu [a,b], Jin Zheng [a,b], Xiangcheng Chen [b], Kexing Song [c,*], Lei Lu [b,*]

[a] School of Materials Science and Engineering, University of Science and Technology of China, Shenyang 110016, China
[b] Shenyang National Laboratory for Materials Science, Institute of Metal Research, Chinese Academy of Sciences, Shenyang 110016, China
[c] Institute of Materials, Henan Academy of Sciences, Zhengzhou 450002, China

ARTICLE INFO

Keywords:
Electrodeposited Cu foils
Sodium saccharin
Microstructure
Strength and elongation
Electrochemical mechanism

ABSTRACT

Electrodeposited copper foils with engineered properties are in high demand as critical components in lithium-ion batteries (LIBs) and printed circuit boards (PCBs). In this study, the effects of sodium saccharin (SAC) on the 9 μm-thick electrodeposited copper foils were systematically investigated. SAC is found to markedly reduce the surface roughness of the copper foils, attaining a minimum Rz value of 0.91 μm. As the SAC concentration increases, the grain size of the copper foils decreases markedly, accompanied by an enhancement in dislocation density. Moreover, the (220) crystallographic texture becomes increasingly pronounced. These microstructural changes induced by SAC collectively contribute to a significant improvement in mechanical performance, with the tensile strength reaching up to 617 MPa. To elucidate the working mechanism of the electrodeposition additive, a series of electrochemical analyses were conducted, revealing that SAC forms complexes with cupric ions, thereby altering the electrochemical reduction kinetics and elevating the electrodeposition overpotential. Furthermore, SAC exhibits a potential-dependent behavior that stems from the imbalance between the consumption and transport rates of cupric ions during the electrodeposition process. These findings shed light on the role that complexing agents play in electrodeposited copper foil production, providing both mechanistic insight and a practical basis for engineering high-performance electrodeposited copper foils.

1. Introduction

Electrodeposited copper foils have become indispensable in the fabrication of a range of devices, particularly in the manufacturing of lithium-ion batteries (LIBs) [1–3] and printed circuit boards (PCBs) [4–6], owing to their exceptional electrical conductivity, thermal stability, and compatibility with precision patterning processes [7–12]. As device architectures continue to miniaturize for power density enhancement, the demand for thinner, more reliable copper foils has grown substantially. Mechanical strength is essential for ensuring the long-term reliability of electrodeposited copper foils in practical use. In LIBs, copper foils must withstand mechanical stresses encountered during electrode fabrication, cell assembly, and repeated charge-discharge cycles [13,14]. In PCBs, copper foils are subjected to lamination, drilling, and thermal cycling [15,16]. Therefore, high-strength copper foils are crucial for minimizing the risk of tearing, wrinkling, or deformation that could compromise electrical interconnects [17–19]. Surface smoothness is another essential attribute of high-performance copper foils. A smoother copper foil surface reduces interfacial impedance in LIBs by enhancing contact with the active material layer and improves fine-line resolution and signal integrity in PCBs by minimizing surface scattering [20–22].

The mechanical properties and surface roughness of copper foils are strongly influenced by the additives employed during electrodeposition. These Additives can be broadly categorized, based on their functional roles, into adsorptive [23–28] and complexing agents [29–31]. To date, most studies have primarily focused on adsorptive additives, such as gelatin and bis-(3-sulfopropyl)-disulfide [23,26], which increase the electrodeposition overpotential, thereby promoting grain refinement and enhancing the mechanical strength of the deposits. Our

* Corresponding authors.
E-mail addresses: zcheng13s@imr.ac.cn (Z. Cheng), kxsong@mail.haust.edu.cn (K. Song), llu@imr.ac.cn (L. Lu).

https://doi.org/10.1016/j.electacta.2025.147431
Received 13 July 2025; Received in revised form 1 September 2025; Accepted 20 September 2025
Available online 20 September 2025

investigation of 2-mercaptobenzimidazole (MBI) reveals a similar behavior, demonstrating its capability to refine the microstructure and promote nanotwin formation, thus enhancing the overall performance of the resulting copper foils through its adsorption on the cathode surface [24].

Although less frequently studied, complexing agents play a vital role in the electrodeposition process, particularly in the production of metallic electrodeposits with desirable properties. By forming coordination complexes with metal ions in the electrolyte, these agents regulate the electrodeposition overpotential, thereby modulating the reduction kinetics and deposition behavior [29–32]. For instance, the use of five different ligands under identical preparation conditions in nickel plating results in five distinct electrodeposition rates and current efficiencies [32]. Complexing agents not only alter the overpotential required for electrodeposition but also impact the texture of electrodeposits [33–36]. It has been reported that the use of sodium citrate, a complexing agent, as an electrodeposition additive promotes the formation of (111) texture during prolonged deposition [36]. In the context of electrodeposited copper foil fabrication, the ability of complexing agents to regulate deposition kinetics and crystallographic growth is especially valuable, as these factors are directly linked to the mechanical strength and surface quality of the final product [37–41]. Therefore, understanding the role of complexing agents is essential for optimizing electrodeposition conditions and achieving superior copper foil quality.

Currently, the understanding of the working mechanism of complexing agents in electrodeposition is primarily confined to the additional overpotential required to dissociate the complexes formed between metal ions and the complexing agents [30,42–44]. However, to date, a comprehensive mechanistic framework detailing the behavior of complexing agents as electrodeposition additives remains lacking. In particular, the dynamic evolution of metallic species, including free ions and their complexes with electrodeposition additives, under varying electrochemical conditions has yet to be fully elucidated.

In this work, a complexing agent, sodium saccharin (SAC), was utilized as an electrodeposition additive to enhance the mechanical strength and surface quality of 9 μm electrodeposited copper foils. A comprehensive investigation was carried out to elucidate its regulatory effect on the microstructure, with particular attention given to grain refinement, dislocation density, and crystallographic orientation. Surface roughness was also quantitatively assessed, and the corresponding changes in surface morphology were discussed in depth. The findings on the regulatory effects of SAC on the properties of electrolytic copper foils offer a promising strategy for the controlled fabrication of high-quality copper foils. Another key contribution of this study is the in-depth elucidation of the microscopic mechanism by which SAC operates during electrodeposition, achieved through a series of electrochemical experiments. These insights advance the current understanding of complexing agents as additives in electrodeposition processes. It should be noted that the elucidated working mechanism of SAC is not exclusive to this additive alone, but also reflects the general principles governing the behavior of a wide range of complexing agents in electrodeposition systems.

2. Experimental

Electrodeposited copper foils with a nominal thickness of 9 μm were fabricated in a custom-built polypropylene electrodeposited cell. The basic electrolyte consisted primarily of 1.35 mol/L cupric ions (Cu^{2+}) and 2 mol/L hydrogen ions (H^{+}). To investigate the influence of sodium saccharin (SAC) as an additive, its concentration in the electrolyte was precisely controlled by introducing it as a pre-dissolved aqueous solution. Electrodeposition was carried out at a constant temperature of 50 °C, with a current density maintained at 650 mA/cm^2—conditions consistent with those widely adopted in industrial foil manufacturing. A pure titanium plate served as the cathode, while the anode was iridium-coated titanium. During deposition, the cathode was rotated at 500 rpm to enhance electrolyte circulation and mass transport.

Tensile testing was conducted in accordance with IPC-TM-650 2.4.18 standards. The tests were performed on an Instron 68TM-5 universal testing machine using rectangular samples measuring 150 mm in length and 12.7 mm in width. A constant strain rate of 50 mm/min was applied, with a gauge length fixed at 50 mm.

The surface roughness of the matte side of the foils was evaluated using a Marsurf M300 roughness tester. Surface morphology was further examined by scanning electron microscopy (SEM, FEI Verios 460) operating in secondary electron mode. Prior to SEM observation, all specimens underwent cleaning with 10 % sulfuric acid solution followed by rinsing in deionized water. To analyze the cross-sectional structure, electrodeposition was employed to coat each sample with an approximate 2 mm-thick copper protective layer, then subjected to a combination of mechanical polishing and electropolishing. The electropolishing procedure was carried out at room temperature using an electrolyte comprising 25 % phosphoric acid, 25 % ethanol, and 50 % deionized water. Cross-sectional imaging was performed using SEM in backscattered electron mode. The average grain size was statistically determined using the intercept method based on the measurements of the lateral dimension of approximately 300 grains. Electron backscatter diffraction (EBSD) was conducted using an FEI Nova 450 SEM, with an accelerating voltage of 20 kV. The resistivity of the copper foils was tested by a four-probe tester (FT-361A). The copper foils underwent a heat treatment process within an atmospheric box furnace at 150 °C for 10 min. The crystallographic texture of the matte side of the foils was characterized by X-ray diffraction (XRD, Bruker D8 Advance). The texture coefficient (TC) was calculated using the following formula:

$$TC(hkl) = \frac{I(hkl)}{I_0(hkl)} \Big/ \frac{1}{n}\sum_{hkl}\frac{I(hkl)}{I_0(hkl)} \tag{1}$$

Here, $TC(hkl)$ denotes the texture coefficient corresponding to a specific crystallographic plane (hkl), $I(hkl)$ refers to the measured relative intensity of that plane, $I_o(hkl)$ represents the standard intensity obtained from JCPDS powder diffraction data, and n indicates the total number of diffraction peaks considered. The X-ray diffraction analysis was carried out using Cu Kα radiation (λ = 1.5418 Å), with scans performed over the 2θ range of 20° to 100° at a rate of 1.5° /min.

Electrochemical characterization was conducted in a standard three-electrode glass cell connected to a Metrohm VIONIC electrochemical workstation. All tests were performed in a basic electrolyte containing 0.5 mol/L Cu^{2+} and 2 mol/L H^{+} at 25 °C. The reduced cupric ion concentration and lowered temperature were chosen to improve the clarity and resolution of the electrochemical responses. A platinum plate was used as the counter electrode, while the reference electrode was a mercury(I) sulfate electrode (MSE). Unless otherwise stated, all reported working electrode potentials E are referenced to MSE. The working electrode was a glassy carbon rotating disk electrode (GC-RDE) with a diameter of 5 mm. Prior to each electrochemical experiment, a 7 μm-thick copper layer was electrodeposited onto the surface of the RDE using the base electrolyte, creating a copper working electrode. During measurements, the electrode was rotated at a fixed speed of 100 rpm. Linear sweep voltammetry (LSV) was performed by scanning from the open circuit potential toward −1 V at a scan rate of 5 mV/s. Electrochemical impedance spectroscopy (EIS) was carried out at $E = -0.55$, −0.60, and −0.65 V, using a sinusoidal perturbation of 10 mV amplitude over a frequency range $0.01 \le f \le 10^5$ Hz. The potential ranges applied in this study do not overlap with that of hydrogen evolution, thereby ensuring that hydrogen evolution is completely excluded from influencing the observed electrochemical behavior.

3. Results

3.1. Surface morphology and microstructure evolution with SAC concentration

Fig. 1 presents SEM images illustrating the surface morphologies of copper foil electrodeposited with varying concentrations of SAC. In the absence of SAC (Fig. 1(a)), the copper surface exhibits a nodular, heterogeneous morphology characterized by the coexistence of large cauliflower-like agglomerates and smaller crystallites. These crystallites are loosely packed, resulting in a surface with distinct crevices extending between the crystallites. Upon the addition of 50 ppm SAC (Fig. 1(b)), the surface becomes noticeably more compact, with a higher degree of grain coalescence. The crystallites appear finer and more uniformly distributed. As the SAC concentration increases further (Fig. 1(c, d)), the surface evolves toward greater smoothness and homogeneity. The grains become more refined and closely packed, resulting in a flatter and denser morphology. Additionally, the addition of SAC results in the formation of tower-shaped crystallites on the surface of the copper foils. The surface coverage of the crystallite increases from 4.72×10^{-4} at 50 ppm SAC to 1.01×10^{-3} at 200 ppm SAC.

The corresponding quantitative surface roughness values are shown in Fig. 1(e). The surface roughness (Rz) decreases monotonically with increasing SAC concentration, from 2.15 μm at 0 ppm to 0.91 μm at 200 ppm. This trend is consistent with the progressive morphological refinement observed in the SEM images and further confirms the surface-smoothing effect of SAC.

The cross-sectional SEM images in Fig. 2(a–d) show the evolution of copper foil microstructures with increasing concentrations of SAC in the electrolyte. In the absence of SAC (Fig. 2(a)), the microstructure is characterized by a mixture of large, elongated columnar grains extending vertically along the thickness of the foil and smaller equiaxed grains. With the introduction of 50 and 100 ppm SAC (Fig. 2(b, c)), the copper grains become notably finer, with a reduction in the proportion of columnar grains. Further increasing the SAC concentration to 200 ppm (Fig. 2(d)) leads to a significant transformation of the microstructure, showing uniformly refined grains.

Fig. 2(e) quantitatively presents the average grain size as a function of SAC concentration. A clear decreasing trend is observed: the average grain size decreases progressively from approximately 423 nm at 0 ppm to 251 nm at 200 ppm SAC. These results confirm that increasing the SAC concentration leads to a refinement of the copper foil grain structure.

As shown in Fig. 3(a), the matte side of the copper foils exhibits distinct XRD peaks corresponding to the (111), (200), and (220) crystal planes, characteristic of the copper FCC structure. Notably, the relative intensity of the (220) peak shows an overall increasing trend with rising SAC concentrations, indicating that SAC promotes the preferential growth of grains exhibiting (220) orientation. Fig. 3(b) quantifies this texture evolution using texture coefficients (TCs). The TC for the (220) plane rises significantly from 1.28 at 0 ppm SAC to 1.82 at 200 ppm SAC, confirming the enhanced preferential orientation. Conversely, the TCs for the (111) and (220) planes exhibit a general decreasing trend. Specifically, the TCs for (111) and (200) are 1.21 and 0.51 at 0 ppm SAC, respectively, but drop to 0.81 and 0.36 at 200 ppm SAC, indicating suppression of these orientations at elevated SAC concentrations. The results demonstrate a clear correlation between SAC concentration and the development of a (220)-dominated texture.

The microstructure of copper foils prepared without SAC and with 200 ppm SAC was characterized by EBSD, as shown in Fig. 4. The Inverse Pole Figures (IPFs) (Fig. 4(a, e)) reveal notable differences in crystallographic texture. The 0 ppm SAC sample exhibits a relatively weak and dispersed texture, whereas the 200 ppm SAC sample shows a pronounced (110) texture, which is consistent with the XRD analysis. The orientation maps (Fig. 4(b, f)) reveal that SAC significantly refines the grain structure, indicating that SAC acts as an effective grain refiner. Kernel Average Misorientation (KAM) maps shown in Fig. 4(c, g) reveal the degree of local lattice distortion. The dislocation density is 10.89×10^{16} m^{-2} and 13.6×10^{16} m^{-2} for the 0 ppm and 200 ppm SAC samples, respectively. Grain boundary maps (Fig. 4(d, h)) differentiate high-angle grain boundaries (HAGBs, black lines) from low-angle grain boundaries (LAGBs, red lines). According to the maps, the addition of SAC leads to an increase in LAGBs from 7.6 % to 9.8 %, consistent with the observed increase in dislocation density.

3.2. Mechanical properties

Fig. 5 presents the effect of SAC concentration on the mechanical properties of electrodeposited copper foils. As shown in the tensile stress–strain curves (Fig. 5(a)), the addition of SAC leads to an enhancement in tensile strength compared to the SAC-free sample. The tensile strength increases progressively with SAC concentration, reaching a maximum at 200 ppm, with the tensile strengths at 50 ppm and 100 ppm SAC remaining comparable. Correspondingly, as summarized in Fig. 5(b), the tensile strength rises from 548 MPa (0 ppm SAC) to a peak of 617 MPa (200 ppm SAC), while the values for the copper foils prepared with 50 ppm and 100 ppm SAC are 578 MPa and 580 MPa, respectively. The addition of SAC slightly reduces the elongation of the

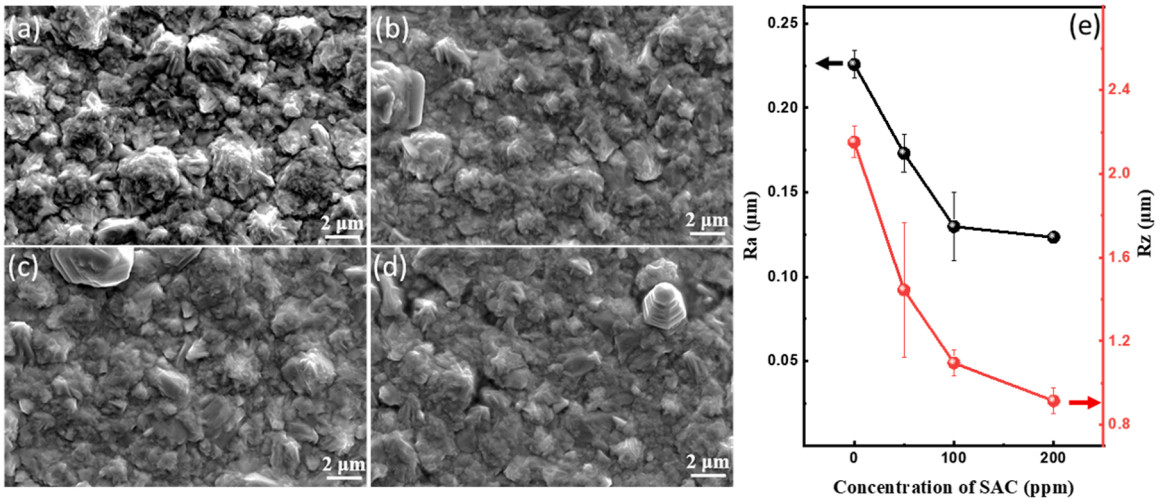

Fig. 1. (a-d) Surface morphologies of copper foils prepared with varying concentrations of SAC: (a) 0 ppm, (b) 50 ppm, (c)100 ppm, (d) 200 ppm. (e) Variation of surface roughness with SAC concentration.

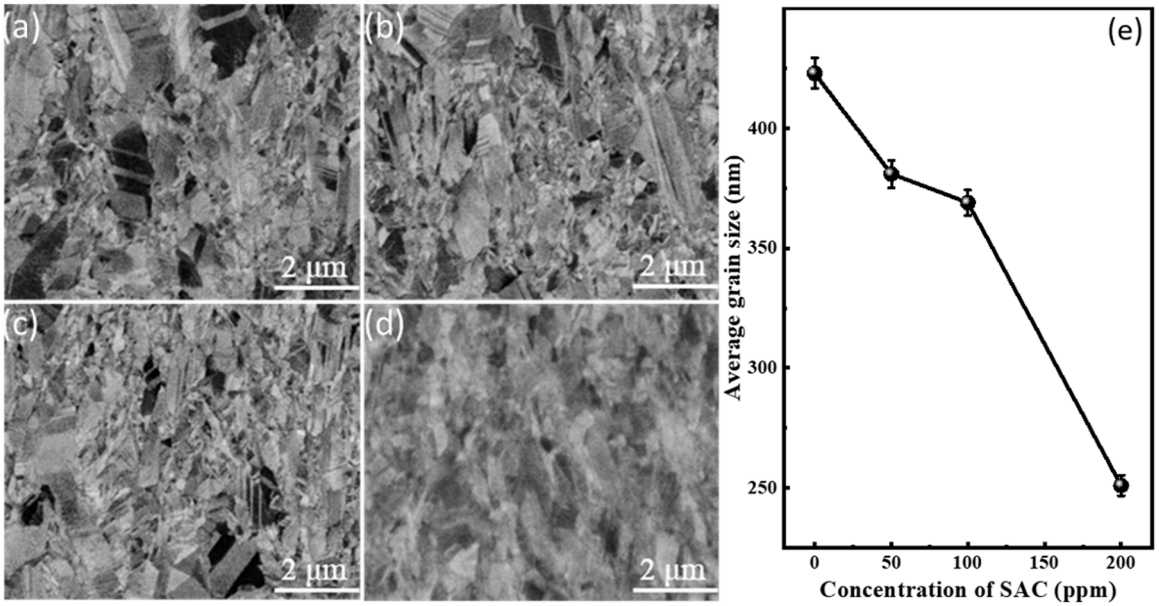

Fig. 2. (a-d) Cross-sectional SEM images showing the microstructures of copper foils prepared with varying concentrations of SAC: (a) 0 ppm, (b) 50 ppm, (c) 100 ppm, (d) 200 ppm. (e) Variation of average grain size with SAC concentration.

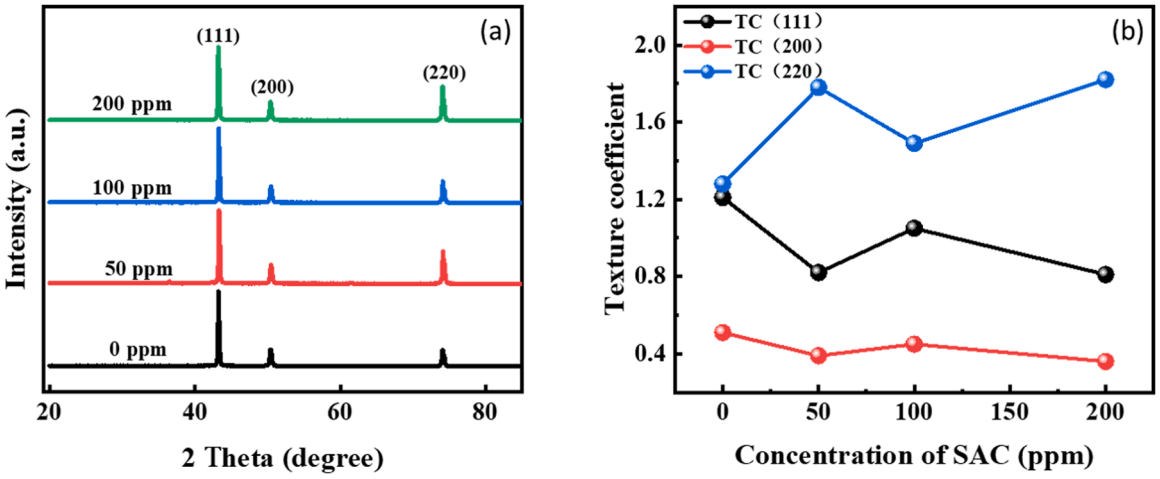

Fig. 3. (a) XRD patterns and (b) texture coefficients of copper foils prepared with varying concentrations of SAC.

copper foils. The SAC-free sample exhibits the highest elongation, reaching 4.2 %, while the SAC-prepared foils show comparable but lower elongation values, all ranging around 3–3.5 %.

3.3. Electrical conductivity and thermal stability

Fig. 6 presents the electrical conductivity and resistivity of copper foils prepared with different concentrations of SAC. The measurement reveals that the conductivity decreases slightly from 59.07 MS/m (101.8 % IACS) to 55.84 MS/m (96.3 % IACS) as the SAC concentration increases from 0 ppm to 200 ppm. Correspondingly, the resistivity increases slightly from 1.69 μΩ·cm to 1.79 μΩ·cm over the same concentration range. While the decrease in conductivity is observable, its extent remains small; even at the highest SAC concentration examined (200 ppm), the foils retain >94 % of the conductivity of the foil prepared without SAC, demonstrating that the electronic transport properties of copper foils are scarcely affected by SAC.

Fig. 7 presents the tensile stress–strain curves of the annealed copper foils, as well as the comparison of tensile strength between as-deposited and annealed copper foils. As shown in Fig. 7(a), the tensile strength of the annealed foils decreases progressively with increasing SAC concentration, showing a slight decline from 513 MPa at 0 ppm SAC to 508 MPa at 50 ppm, followed by a more pronounced reduction to 487 MPa at 100 ppm, and eventually to 464 MPa at 200 ppm. Notably, even under this relatively severe annealing condition for 9 μm-thick copper foils, the sample prepared with 200 ppm SAC still retains a comparatively high tensile strength of 464 MPa. The comparison of tensile strength is presented in Fig. 7(b), showing that the heat treatment leads to a more pronounced strength loss at higher SAC concentrations. This behavior can be attributed to SAC-induced grain refinement, as smaller grain sizes typically exhibit lower thermal stability.

4. Discussion

Through a combination of SEM, XRD, EBSD, and mechanical testing, SAC is identified as an effective surface-smoothing agent and grain refiner in the preparation of electrodeposited copper foil. Consequently, the resulting copper foil exhibits markedly improved surface quality and

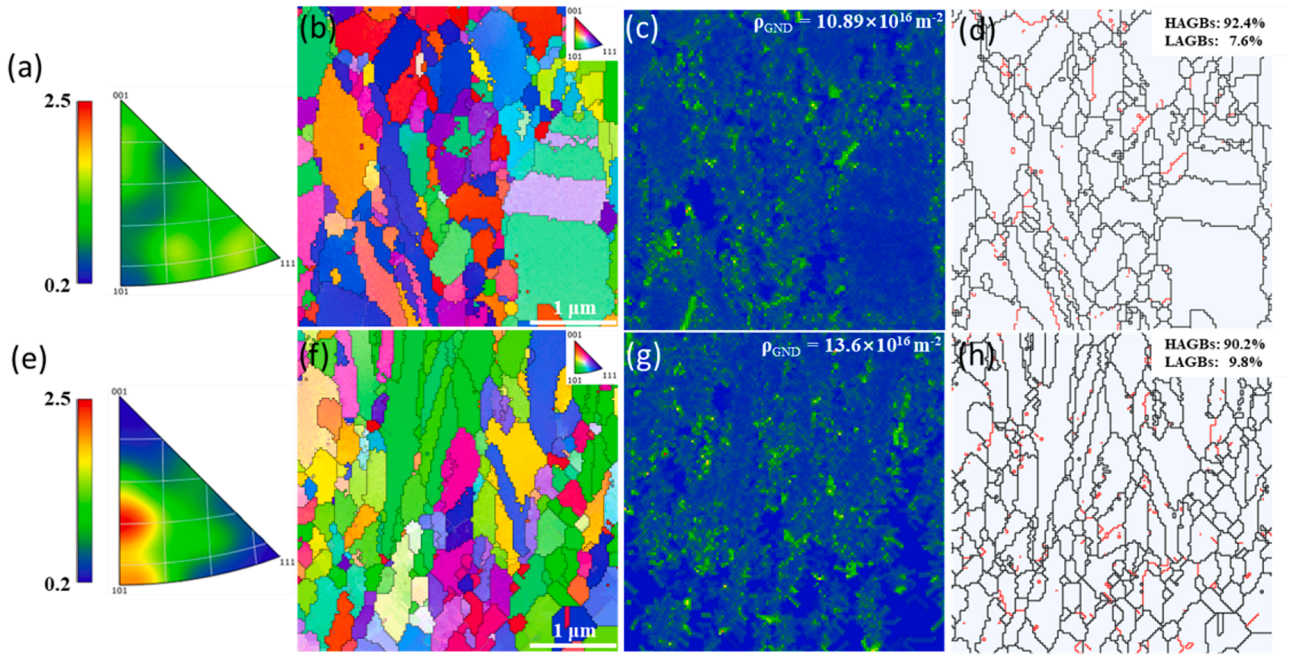

Fig. 4. EBSD analysis of copper foils prepared with 0 ppm and 200 ppm SAC. (a, e) Inverse Pole Figures (IPF), (b, f) orientation maps, (c, g) Kernel Average Misorientation (KAM) maps with dislocation density indicated, and (d, h) grain boundary maps showing the fractions of high-angle grain boundaries (HAGBs, black lines) and low-angle grain boundaries (LAGBs, red lines). Top row (a–d): 0 ppm SAC; bottom row (e–h): 200 ppm SAC.

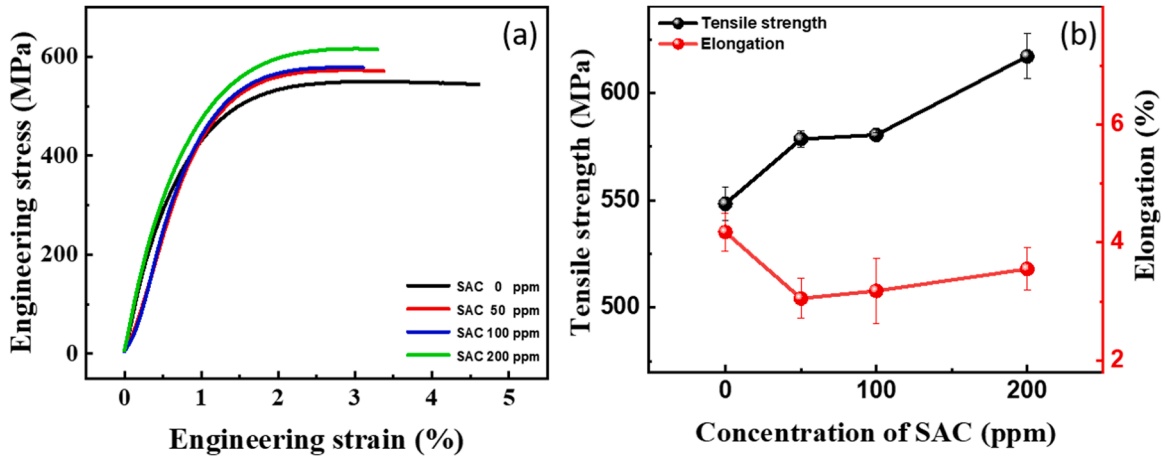

Fig. 5. (a) Tensile stress-strain curves and (b) tensile strength and elongation of copper foils prepared with varying concentrations of SAC.

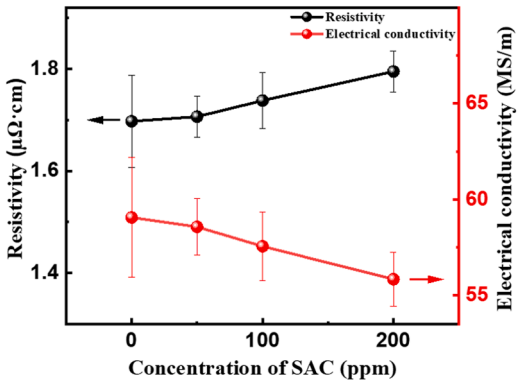

Fig. 6. Electrical conductivity and resistivity of copper foils prepared with varying concentrations of SAC.

mechanical strength. To uncover the fundamental reasons behind these enhancements, the following section presents a detailed discussion of SAC's role in modulating surface morphology and strengthening the copper foils. Particular emphasis is placed on the working mechanism of SAC, which is regarded as the primary factor leading to the observed enhancement in foil properties.

4.1. *Electrochemical analysis and working mechanism of SAC*

Fig. 8 shows the LSV curves obtained at various SAC concentrations. At 0 ppm SAC, the curve distinctly exhibits the three typical kinetic regions as the potential of the working electrode is swept in the negative direction. Initially, from approximately −0.39 V (OCP) to −0.6 V, the charge transfer (i.e., the reduction of cupric ions) is sluggish, indicating a region where activation control dominates. As the potential becomes more negative and the current density reaches its maximum, the process becomes entirely diffusion-controlled (from around −0.8 V onwards), with the transport of Cu^{2+} ions to the electrode surface being the rate-

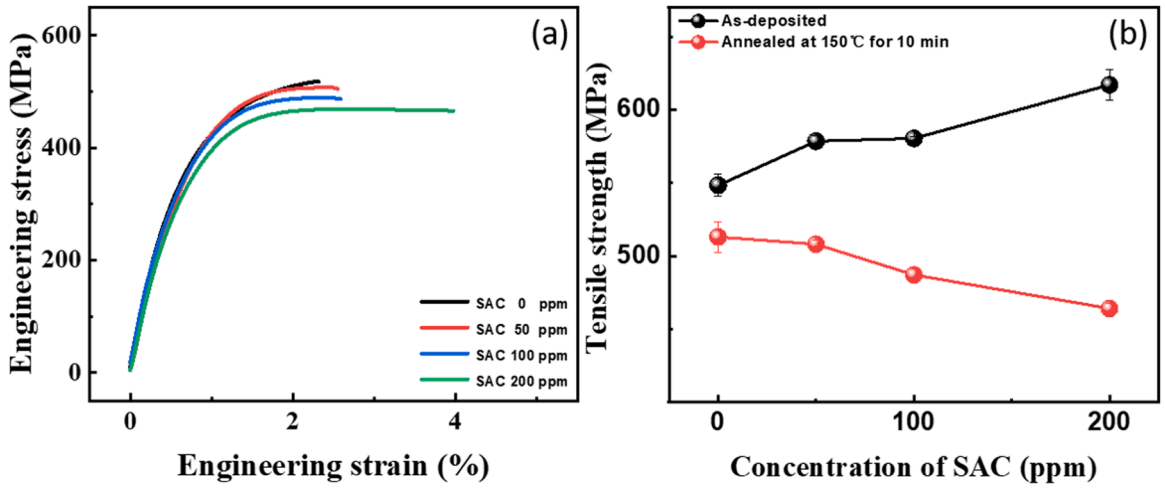

Fig. 7. (a) Tensile stress-strain curves of copper foils prepared with varying concentrations of SAC after annealing at 150 °C for 10 min. (b) Tensile strength comparison between as-deposited and annealed copper foils prepared with varying SAC concentrations.

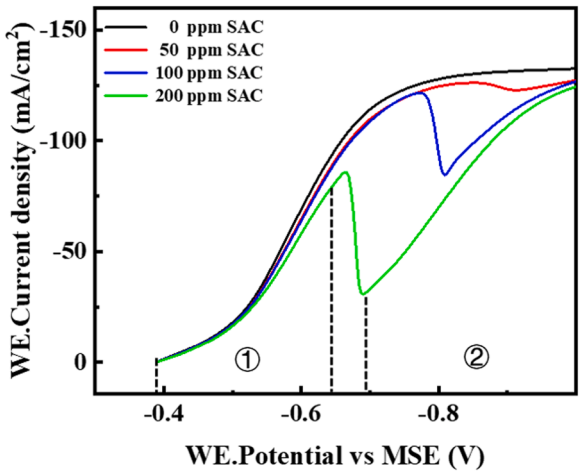

Fig. 8. Linear sweep voltammetry at various SAC concentrations.

limiting step. Between these two regions, from −0.6 V to −0.8 V, lies a mixed control region where both charge transfer and mass transport influence the overall rate.

With the addition of SAC, a distinct peak appears in the LSV curves for all three SAC concentrations examined in this study. Notably, the peak potential shifts positively with increasing SAC concentration, from approximately –0.80 V at 50 ppm to –0.65 V at 200 ppm. When the electrode potential is more negative than the peak potential, the reduction reaction is only mildly suppressed across all concentrations, with the degree of suppression gradually increasing as the potential becomes more negative. However, beyond the peak, the electrode reaction becomes significantly inhibited, and this inhibition intensifies with higher SAC concentrations.

This peak is typically attributed to the onset of a diffusion-controlled process; during this process, the charge transfer rate exceeds the mass transport rate of free cupric ions, resulting in depletion of cupric ions near the electrode surface. However, rather than reaching a plateau, the current density continues to increase with further negative polarization. This behavior, together with the pronounced suppression of the reduction reaction beyond the peak, implies a change in the composition of the electroactive species. The most plausible explanation is the formation of cupric ion–SAC complexes, which shifts the nature of the reactive species from predominantly free cupric ions to a mixture of free ions and coordination complexes. Although the precise chemical structure of the cupric ion–SAC complex under the specific electrochemical conditions of copper electrodeposition has not yet been fully elucidated, the interpretation of SAC acting as a complexing agent is in good agreement with previous studies [45–47].

Prior to the diffusion peak, the rate of the electrode reaction is largely unaffected, since mass transport can replenish free cupric ions at a rate sufficient to sustain the cupric ion reduction reaction. However, when the potential is more negative than the diffusion peak potential, the consumption of free cupric ions outpaces their transport to the electrode surface. Once the free cupric ions are largely depleted in the vicinity of the electrode surface, the spaces once occupied by cupric ions are dominated by the cupric ion-SAC complexes, leading to a significant increase in the proportion of the complex in the reactant mixture. Since the reduction of the Cupric ion-SAC complexes requires more energy than that of free cupric ions, the post-peak region exhibits the observed significant suppression in current. For clarity, the pre- and post-peak regions of the 200 ppm SAC LSV curve are denoted as regions ① and ② in Fig. 8.

As evidenced by the LSV results, the addition of SAC significantly alters the electrochemical behavior of the system by complexing with cupric ions. This interaction, under negative polarization, induces a transition in the dominant electroactive species from free cupric ions to a mixed population comprising free cupric ions and cupric ion–SAC complexes, thereby increasing the overpotential required for reduction and impeding the overall electrode reaction. The characteristic features of the LSV curves—namely, the appearance of a diffusion peak, the post-peak current suppression—are all consistent with this mechanistic interpretation.

The above discussions are further validated and deepened by the EIS results. The Nyquist plots for 0, 100, and 200 ppm SAC at working electrode potentials of –0.55, –0.6, and –0.65 V are presented in Fig. 9(a-i), while the equivalent circuits used for fitting the EIS data are shown in Fig. 9(j). The equivalent circuits consist of constant phase elements (CPE), resistors (R), and a Warburg element (W_s), with the corresponding fitting parameters listed in Table 1. Specifically, R_s, R_{ct}, and R_2 represent the solution resistance, the resistance associated with cupric ion reduction, and the resistance of another electrode process responsible for the second capacitive loop with a larger time constant, respectively. The capacitances corresponding to the cupric ion reduction and the other electrode process are denoted as C_{dl} and C_2, respectively. The Warburg resistance associated with diffusion is labeled as R_w.

For the blank electrolyte (Fig. 9(a–c)), only a single capacitive loop is observed, followed by a typical finite-length diffusion behavior (a straight line transitioning into a loop) at all three working electrode

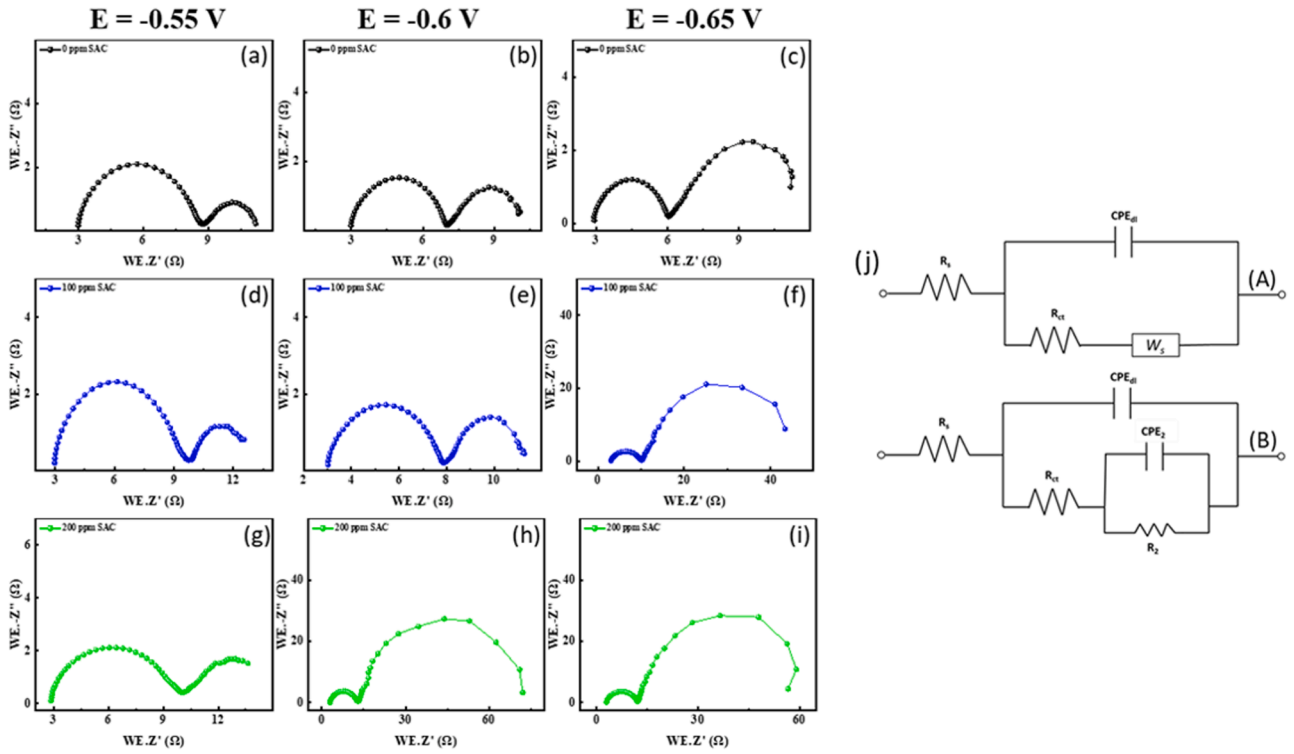

Fig. 9. Nyquist plot for (a-c) 0 ppm, (d-f) 100 ppm, and (g-i) 200 ppm SAC at E= −0.55 V, −0.6 V, and −0.65 V. (j) Equivalent circuits utilized to fit experimental EIS: (A) for (a-d), (g); (B) for (e), (f), (h), and (i).

Table 1
Parameters used for EIS data fitting.

Working electrode potential	SAC concentration	R_s (Ω)	R_{ct} (Ω)	C_{dl} (μF)	R_2 (Ω)	C_2 (mF)	R_w(Ω)
- 0.55 V	**0 ppm**	2.92	5.58	7.36	—	—	2.85
	100 ppm	2.82	6.67	7.8	—	—	3.28
	200 ppm	2.7	6.84	12.28	—	—	10.37
- 0.6 V	**0 ppm**	2.93	3.99	9.2	—	—	3.32
	100 ppm	2.9	5.02	9.8	3.64	385.52	—
	200 ppm	2.86	10.37	11.38	55.5	228.91	—
- 0.65 V	**0 ppm**	2.85	3.21	11.96	—	—	5.95
	100 ppm	2.9	7.37	10.62	39.17	203.47	—
	200 ppm	2.85	9.54	10.21	51.82	131.97	—

potentials. As summarized in Table 1, the resistance for cupric ion reduction (R_{ct}) progressively decreases from 5.58 Ω at –0.55 V to 3.21 Ω at –0.65 V as the working electrode potential becomes more negative, reflecting the lowering of the activation energy barrier. In addition, the Warburg resistance (R_W) increases from 2.85 Ω to 5.95 Ω over the same potential range, indicating the increased demand on mass transport due to enhanced cupric ion reduction rate.

When the SAC concentration is 100 ppm (Fig. 9(d–f)), the Nyquist plot exhibits finite-length diffusion behavior only at –0.55 V. At higher working electrode potentials (–0.6 V and –0.65 V), a well-defined capacitive loop emerges at low frequencies. As the potential shifts from –0.55 V to –0.6 V, the resistance of the first capacitive loop (R_{ct}) decreases from 6.67 Ω to 5.02 Ω. Counterintuitively, R_{ct} increases to 7.37 Ω at –0.65 V, suggesting that the reactant for the first capacitive loop is no longer solely cupric ions but a mixture of free cupric ions and cupric ion-SAC complexes, with cupric ions remaining the predominant reduced electroactive species. At –0.6 V, the resistance of the second capacitive loop is only 3.64 Ω, suggesting that the associated electrode process does not arise from the reduction of either free cupric ions or the reactant mixture. Rather, it is attributed to the adsorption of cupric ion-SAC complexes onto the electrode surface, since the complexes have a lower diffusion coefficient compared to free cupric ions. At –0.65 V, the resistance associated with the second capacitive loop (R_2) reaches 39.17 Ω, indicating a significant contribution of cupric ion-SAC complexes to the electrochemical process. In other words, at –0.65 V, both capacitive loops correspond to the reduction of the mixed reactants, with the second loop involving a significantly higher proportion of cupric ion-SAC complexes.

At 200 ppm SAC (Fig. 9(g–i)), the Nyquist plots show similar behavior to those at 100 ppm. At –0.55 V, finite-length diffusion dominates at low frequencies. However, at –0.6 V and –0.65 V, a large capacitive loop appears at low frequencies, with resistances of 55.5 Ω and 51.82 Ω, respectively, indicating an even greater proportion of cupric ion–SAC complexes in the reduced reactant mixture, as expected with the higher SAC concentration.

At –0.55 V, the resistance of the first capacitive loop R_{ct} slightly increases from 5.58 Ω at 0 ppm SAC to 6.84 Ω at 200 ppm SAC. This trend reflects the transition of the reduced reactant from pure cupric ions to a mixture containing a growing but still negligibly small proportion of cupric ion-SAC complexes. The slight increase in R_{ct} with SAC concentration aligns with the minor inhibition observed before the diffusion peak in the LSV curves. Additionally, it is noteworthy that the Warburg resistance (R_W) rises from 2.85 Ω at 0 ppm SAC to 10.37 Ω at 200 ppm SAC at –0.55 V, further confirming the formation of complexes between

cupric ions and SAC molecules.

The electrochemical analyses collectively point to a mechanistic framework in which the inhibitory effect of SAC arises from its ability to form complexes with cupric ions, thereby altering the composition of electroactive species in the vicinity of the electrode surface. This effect is distinctly potential-dependent. At potentials more positive than a critical value, the reduction predominantly involves free cupric ions, and the presence of SAC exerts minimal influence. However, at potentials more negative than the critical value, the consumption of free cupric ions surpasses their diffusion replenishment, leading to a significant increase in the proportion of cupric ion–SAC complexes among the reduced electroactive species. As a result, the electrodeposition process is markedly hindered due to a more negative reduction potential required for the complexes. It should be noted that the critical potential is concentration-dependent, with higher SAC concentrations shifting the critical potential toward more positive values, whereas lower concentrations produce the opposite effect. Fig. 10 illustrates the composition of the electroactive species at the cathode surface at electrodeposition potentials both more positive and more negative than the critical potential with SAC as the electrodeposition additive. It should be emphasized that the elucidated working mechanism is not only applicable to SAC but also extends to a wide range of complexing agents commonly employed in electrodeposition.

4.2. Regulatory effect of SAC on nucleation mechanism and surface morphology

The coarse cauliflower-like agglomerates observed in Fig. 1(a) are characteristic of uncontrolled three-dimensional growth, which typically arises from locally elevated current densities at the cathode surface. Such morphological features reflect the presence of inhomogeneous electric fields and uneven surface energy distribution, leading to preferential nucleation and accelerated growth at certain surface features such as protruding or defect-rich sites. Additionally, the pronounced heterogeneity in crystallite size further suggests a nonuniform distribution of active sites for nucleation. These phenomena discussed above are likely due to the absence of adsorption-mediated regulation on the electrode surface properties during the electrodeposition process.

Upon the introduction of SAC, a marked enhancement in surface morphology uniformity is observed. This can be attributed to the formation of cupric ion–SAC complexes in the electrolyte, which exhibit a preferential adsorption behavior on high-energy regions of the cathode surface, such as protrusions, step edges, or defect sites. The selective adsorption of these complexes acts to homogenize the electrochemical activity across the substrate surface, effectively equalizing the availability of active nucleation sites. This redistribution of surface reactivity leads to the suppression of localized current density spikes, thereby mitigating the development of cauliflower-like agglomerates and promoting a more uniform grain size distribution. Furthermore, the formation of cupric ion–SAC complexes increase the electrodeposition overpotential, which in turn promotes a higher nucleation rate, thereby leading to a refinement in crystallite size.

According to [48], the work of formation of a critical nucleus with a specific geometry and crystallographic texture is closely related to the overpotential. When the work of formation of certain texture is lower than that of others, the electrodeposits tend to develop that texture. In the case of electrodeposited copper foils, it is thus reasonable to infer that under electrodeposition conditions modified by the addition of SAC, particularly changes in overpotential, the (220)-oriented nuclei attain their critical size with the lowest formation energy. Consequently, the presence of SAC promotes the development of the (220) texture.

4.3. Formation mechanism of the tower-shaped crystallites

With the addition of SAC, tower-shaped crystallites begin to emerge on the surface of the copper foils. These crystallites are not densely distributed across the surface, which can be attributed to the progressive nucleation mechanism. Under this mechanism, the majority of nuclei grow and coalesce, forming larger grains or crystallite clusters. Moreover, it is common for new nuclei to emerge on the surface of growing ones, further promoting merging. As a result, only those nuclei that form in relatively isolated regions, free from interference by neighboring or newly forming nuclei, are able to develop fully into the characteristic tower-like geometry. Consequently, the tower-shaped crystallites appear sparsely across the copper surface. Notably, such crystallites are observed only after the introduction of SAC as an electrodeposition additive, indicating that SAC plays a critical role in promoting their formation. The following section will elaborate on the underlying formation mechanism of these tower-shaped nuclei.

The tower-shaped nucleus can be divided into two structural components: the tower body and the tower tip, as shown in Fig. 11. The tower tip (Fig. 11(a)) exhibits the morphology of a flattened hexagonal pyramid. Given that SAC promotes the development of a (220) texture, the basal face of this hexagonal pyramid is identified as the (220) crystallographic plane. Based on the geometry illustrated in Fig. 11(b), the remaining exposed facets of the pyramid can be crystallographically determined. Regarding the formation mechanism of the tower tip,

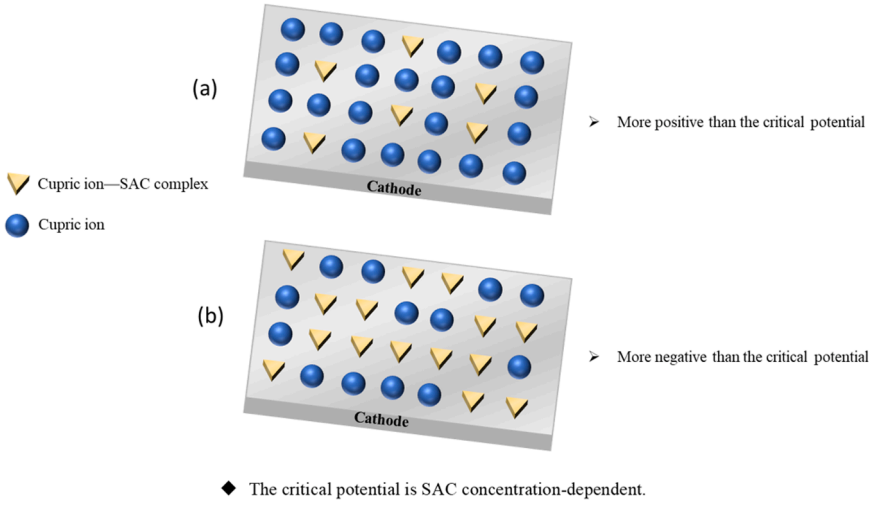

Fig. 10. Composition of electroactive species at the cathode surface at electrodeposition potentials (a) more positive and (b) more negative than the critical potential with SAC as the electrodeposition additive.

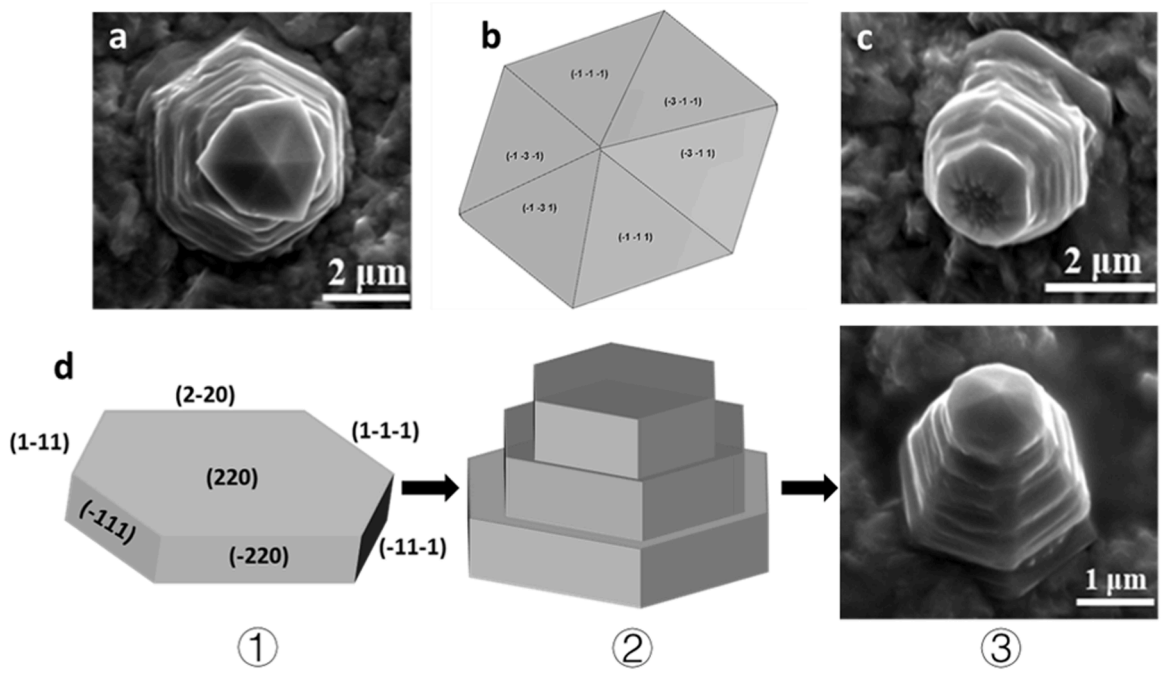

Fig. 11. (a) SEM image of the tip of a tower-shaped crystallite; (b) schematic illustration showing the crystallographic orientation of the exposed facets of the tower tip; (c) SEM image of a tower-shaped crystallite with an incompletely developed tip; (d) proposed formation mechanism of tower-shaped crystallites.

Fig. 11(c) clearly reveals an incompletely formed tower tip, which results from the diffusion of copper atoms toward the center. In this case, diffusion ceased before the migrating atoms fully converged at the center, leaving the tip formation incomplete.

The tower body exhibits the geometry of a hexagonal frustum that is constructed through the vertical stacking of flattened hexagonal prism nuclei. The crystallographic planes corresponding to the surfaces of these prism nuclei are identified as presented in Fig. 11(d①). SAC promotes the formation of such flattened hexagonal prism nuclei, which primarily grow laterally, indicating a two-dimensional growth mode. As growth proceeds, newly formed prism nuclei nucleate on the top surface of existing ones (Fig. 11(d②)) and expand in a similar lateral fashion. Through repeated nucleation and vertical stacking of these prism nuclei, the hexagonal frustum-shaped tower body develops. This formation of the tower body is followed by surface atom diffusion, which promotes the growth of the tower tip; together, these two processes ultimately give rise to the formation of tower-shaped crystallites.

4.4. SAC-induced improvement in copper foil strength

The evolution of mechanical strength in the copper foils is closely correlated with their microstructural characteristics, as revealed by the SEM and EBSD analyses. As shown in the cross-sectional SEM images (Fig. 2(a–d)), increasing the concentration of SAC results in a progressive refinement of the grain structure, with grains becoming smaller and more equiaxed. This refinement leads to a higher density of grain boundaries, which act as barriers to dislocation motion and thereby enhance the material's strength through the grain boundary strengthening mechanism [49,50].

Moreover, the EBSD-derived Kernel Average Misorientation (KAM) maps (Fig. 5(c, g)) reveal an increase in dislocation density with rising SAC concentration, thereby contributing to the enhancement of the mechanical strength of the copper foils [51,52]. In addition, the enhancement of the (110) texture further promotes strength improvement, as its Schmid factor for dislocation activation is lower than that of other orientations (e.g., (100) and (111)), implying a higher yield strength under tensile loading.

5. Conclusion

The application of SAC as an electrodeposition additive presents a promising strategy for enhancing the quality of electrodeposited copper foils. Its incorporation markedly refines the surface morphology and grain structure, resulting in enhanced surface quality and microstructural uniformity. In parallel, elevated SAC concentrations promote the development of (220) crystallographic texture and lead to a higher dislocation density. Mechanically, SAC contributes to a notable improvement in the tensile strength of electrodeposited copper foils, reaching up to 617 MPa at 200 ppm SAC. Electrochemical analyses reveal that SAC interacts with cupric ions through complexation, modifying the reduction kinetics and increasing the overpotential required for electrodeposition. Furthermore, SAC, as an electrodeposition additive, exhibits a potential-dependent behavior that originates from the dynamic interplay between the consumption and transport of cupric ions during electrodeposition. These mechanistic insights, together with SAC's modulating effect on copper foil properties, underscore its strong potential for advancing the quality and reliability of electrodeposited copper foils in practical electrodeposition processes. Further investigations will focus on combining SAC with surface-adsorbing additives to further enhance the performance of electrodeposited copper foils.

CRediT authorship contribution statement

Che Liu: Writing – review & editing, Writing – original draft, Methodology, Investigation, Formal analysis, Conceptualization. **Zhao Cheng:** Writing – review & editing, Supervision, Methodology, Investigation, Formal analysis, Conceptualization. **Linhai Liu:** Methodology, Investigation, Formal analysis. **Jin Zheng:** Methodology, Investigation, Formal analysis. **Xiangcheng Chen:** Methodology, Investigation, Formal analysis. **Kexing Song:** Writing – review & editing, Resources, Conceptualization. **Lei Lu:** Writing – review & editing, Supervision, Resources, Conceptualization.

Declaration of competing interest

The authors declare that they have no known competing financial interests or personal relationships that could have appeared to influence the work reported in this paper.

Acknowledgements

We acknowledge financial support from the National Natural Science Foundation of China (NSFC), Grant No 92163202, 92463302, U24A2027, 52422102 & 52371124, U21A2051), the Global Common Challenges Project (Grant No 172GJHZ2023075GC), the Youth Innovation Promotion Association, Chinese Academy of Sciences (CAS), the National Key R&D Program of China (Grant No 2021YFB3400800 and 2024YFA1210600), Henan Province Top Talent Training Program Project (No 244500510020), and Joint Fund of Henan Province Science and Technology R&D Program (No 235200810004).

Data availability

Data will be made available on request.

References

[1] Z. Xiao, J. Chen, J. Liu, T. Liang, Y. Xu, C. Zhu, S. Zhong, Microcrystalline copper foil as a high performance collector for lithium-ion batteries, J. Power. Sources 438 (2019) 226973.
[2] T. Xia, T. Liang, Z. Xiao, J. Chen, J. Liu, S. Zhong, Nanograined copper foil as a high-performance collector for lithium-ion batteries, J. Alloys Compd. 831 (2020) 154801.
[3] L. Yang, W. Weng, H. Zhu, X. Chi, W. Tan, Z. Wang, S. Zhong, Preparing ultra-thin copper foil as current collector for improving the LIBs performances with reduced carbon footprint, Mater. Today Commun. 35 (2023) 105952.
[4] X. Ye, M. De Bonte, J.P. Celis, J. Roos, Role of overpotential on texture, morphology and ductility of electrodeposited copper foils for printed circuit board applications, J. Electrochem. Soc. 139 (6) (1992) 1592.
[5] J. LaDou, Printed circuit board industry, Int. J. Hyg. Env. Health 209 (3) (2006) 211–219.
[6] I. Artaki, M. Papalski, A. Moore, Copper foil characterization and cleanliness testing, Plat. Surf. Finish. 78 (1) (1991) 64–68.
[7] L.L. Lu, H.T. Liu, Z.D. Wang, Q.Q. Lu, Y.J. Zhou, F. Zhou, Y.M. Zhang, W.W. Lu, B. Yang, Q.Q. Zhu, Advances in electrolytic copper foils: fabrication, microstructure, and mechanical properties, Rare Met. (2024) 1–36.
[8] L. Lu, Y. Shen, X. Chen, L. Qian, K. Lu, Ultrahigh strength and high electrical conductivity in copper, Science 304 (5669) (2004) 422–426.
[9] J. Čížek, I. Procházka, M. Cieslar, R. Kužel, J. Kuriplach, F. Chmelík, I. Stulíková, F. Bečvář, O. Melikhova, R.K. Islamgaliev, Thermal stability of ultrafine grained copper, Phys. Rev. B 65 (9) (2002) 094106.
[10] R. Islamgaliev, F. Chmelik, R. Kuzel, Thermal stability of submicron grained copper and nickel, Mater. Sci. Eng.: A 237 (1) (1997) 43–51.
[11] B.V. Sarada, C.L. Pavithra, M. Ramakrishna, T.N. Rao, G. Sundararajan, Highly (111) textured copper foils with high hardness and high electrical conductivity by pulse reverse electrodeposition, Electrochem. Solid-State Lett. 13 (6) (2010) D40.
[12] J. Rickerby, J.H. Steinke, Current trends in patterning with copper, Chem. Rev. 102 (5) (2002) 1525–1550.
[13] C. Dai, Z. Wang, K. Liu, X. Zhu, X. Liao, X. Chen, Y. Pan, Effects of cycle times and C-rate on mechanical properties of copper foil and adhesive strength of electrodes in commercial LiCoO2 LIBs, Eng. Fail. Anal. 101 (2019) 193–205.
[14] J. Zhu, J. Feng, Z. Guo, Mechanical properties of commercial copper current-collector foils, RSC Adv. 4 (101) (2014) 57671–57678.
[15] L. Zheng, C.Y. Wang, Y.X. Song, L. Yang, Y. Qu, P. Ma, L. Fu, A review on drilling printed circuit boards, Adv. Mat. Res. 188 (2011) 441–449.
[16] J. Bath, Lead-free Soldering Process Development and Reliability, John Wiley & Sons, 2020.
[17] H. Merchant, M. Minor, Y. Liu, Mechanical fatigue of thin copper foil, J. Electron. Mater. 28 (1999) 998–1007.
[18] Z. Zhao, H. Fu, R. Tang, B. Zhang, Y. Chen, J. Jiang, Failure mechanisms in flexible electronics, Int. J. Smart Nano Mater. 14 (4) (2023) 510–565.
[19] B. Weiss, V. Gröger, G. Khatibi, A. Kotas, P. Zimprich, R. Stickler, B. Zagar, Characterization of mechanical and thermal properties of thin Cu foils and wires, Sens. Actuators A: Phys. 99 (1–2) (2002) 172–182.
[20] J. Zhang, D. Zuo, X. Pei, C. Mu, K. Chen, Q. Chen, G. Hou, Y. Tang, Effects of electrolytic copper foil roughness on lithium-ion battery performance, Metals 12 (12) (2022) 2110.
[21] D. McGregor, B. Adams-Melvin, K. Dietz, Effects of copper foil type and surface preparation on fine line image transfer in primary imaging of printed wiring boards, Trans. IMF 74 (4) (1996) 124–132.
[22] S. Hinaga, M. Koledintseva, P. Anmula, J. Drewniak, Effect of conductor surface roughness upon measured loss and extracted values of PCB laminate material dissipation factor, Proc. IPC (2009) 44–60.
[23] R. Taft, H.E. Messmore, The electrodeposition of copper in presence of gelatin, J. Phys. Chem. 35 (9) (2002) 2585–2618.
[24] C. Liu, X. Chen, Z. Cheng, L. Lu, The effect of 2-mercaptobenzimidazole concentration on the microstructure and mechanical properties of electrodeposited Cu foils, Electrochim. Acta (2025) 146330.
[25] M. Tan, C. Guymon, D.R. Wheeler, J.N. Harb, The role of SPS, MPSA, and chloride in additive systems for copper electrodeposition, J. Electrochem. Soc. 154 (2) (2006) D78.
[26] C.H. Lee, S.C. Lee, J.J. Kim, Bottom-up filling in Cu electroless deposition using bis-(3-sulfopropyl)-disulfide (SPS), Electrochim. Acta 50 (16–17) (2005) 3563–3568.
[27] C. Gu, Y. You, X. Wang, J. Tu, Electrodeposition, structural, and corrosion properties of Cu films from a stable deep eutectics system with additive of ethylene diamine, Surf. Coat. Technol. 209 (2012) 117–123.
[28] T.C. Liu, C.M. Liu, H.Y. Hsiao, J.L. Lu, Y.S. Huang, C. Chen, Fabrication and characterization of (111)-oriented and nanotwinned Cu by DC electrodeposition, Cryst. Growth Des. 12 (10) (2012) 5012–5016.
[29] C. Ramírez, B. Bozzini, J.A. Calderón, Electrodeposition of copper from triethanolamine as a complexing agent in alkaline solution, Electrochim. Acta 425 (2022) 1–9.
[30] Y. Jo, S.M. Kim, E.S. Jeong, K.T. Lee, S. Jin, W.Y. Lee, S.Y. Lee, M.H. Lee, On the role of complexing agents in co-electrodeposition of SnAg alloy with uniform composition, Mater. Sci. Semicond. Process. 166 (2023) 107751.
[31] Y.D. Tsai, C.C. Hu, C.C. Lin, Electrodeposition of Sn–Bi lead-free solders: effects of complex agents on the composition, adhesion, and dendrite formation, Electrochim. Acta 53 (4) (2007) 2040–2047.
[32] K. Mech, Influence of organic ligands on electrodeposition and surface properties of nickel films, Surf. Coat. Technol. 315 (2017) 232–239.
[33] Z. Zhang, W. Hu, Y. Deng, C. Zhong, H. Wang, Y. Wu, L. Liu, The effect of complexing agents on the oriented growth of electrodeposited microcrystalline cuprous oxide film, Mater. Res. Bull. 47 (9) (2012) 2561–2565.
[34] F.H. Su, C.S. Liu, P. Huang, Effect of complexing agents and pH on microstructure and tribological properties of Co–W coatings produced by double pulse electrodeposition, Appl. Surf. Sci. 258 (17) (2012) 6550–6557.
[35] G. Wei, H. Ge, L. Huang, Q. Wu, X. Wang, L. Huang, Influence of complexing agent on the electrodeposited Co–Pt–W magnetic thin films, Appl. Surf. Sci. 254 (11) (2008) 3425–3430.
[36] B. Hong, C.H. Jiang, X.J. Wang, Influence of complexing agents on texture formation of electrodeposited copper, Surf. Coat. Technol. 201 (16–17) (2007) 7449–7452.
[37] J. Hu, B. Fan, Z. Wu, D. Zuo, J. Zhang, Q. Chen, G. Hou, Y. Tang, Research progress on the texture of electrolytic copper foils, J. Electron. Mater. 53 (7) (2024) 3460–3473.
[38] J. Zhang, H. Chen, B. Fan, H. Shan, Q. Chen, C. Jiang, G. Hou, Y. Tang, Study on the relationship between crystal plane orientation and strength of electrolytic copper foil, J. Alloys Compd. 884 (2021) 161044.
[39] C.L. Pavithra, B.V. Sarada, K.V. Rajulapati, M. Ramakrishna, R.C. Gundakaram, T. N. Rao, G. Sundararajan, Controllable crystallographic texture in copper foils exhibiting enhanced mechanical and electrical properties by pulse reverse electrodeposition, Cryst. Growth Des. 15 (9) (2015) 4448–4458.
[40] Y. Sun, L. Huang, H. Xie, B. Liu, Y. Fang, G. Han, J. Liu, High-strength copper foil prepared with 2-mercaptothiazoline by direct current electrodeposition, Electrochim. Acta 466 (2023) 143068.
[41] J. Huang, Y. Luo, Y. Tang, M. Chen, N. Song, Z. Wang, Y. Tan, X. Fan, Preparation of high-strength, high-extensibility, and low-roughness ultrathin twinned copper foil: a study on the application of a novel additive, sodium 2-mercapto-5-benz-imidazole sulfonate, Mater. Today Commun. (2025) 113066.
[42] E. Podlaha, C. Bonhote, D. Landolt, A mathematical model and experimental study of the electrodeposition of Ni-Cu alloys from complexing electrolytes, Electrochim. Acta 39 (18) (1994) 2649–2657.
[43] D. Cook, S. Reeves, W. Zhang, G. Reid, W. Levason, P. Bartlett, J. Dyke, V. Greenacre, Tellurium electrodeposition from tellurium (II) and (IV) chloride salts in dichloromethane, Electrochim. Acta 456 (2023) 142456.
[44] M. Bouroushian, T. Kosanovic, D. Karoussos, N. Spyrellis, Electrodeposition of polycrystalline ZnTe from simple and citrate-complexed acidic aqueous solutions, Electrochim. Acta 54 (9) (2009) 2522–2528.
[45] E.J. Baran, V.T. Yilmaz, Metal complexes of saccharin, Coord. Chem. Rev. 250 (15–16) (2006) 1980–1999.
[46] Z. Yugeng, Spectral and thermal properties of saccharin and saccharin metal complexes, Transit. Met. Chem. 19 (4) (1994) 446–448.
[47] S. Cakır, I. Bulut, Electrochemical and thermal studies of the ternary complex of Cu (II) with saccharin and nicotinamide, J. Electroanal. Chem. 518 (1) (2002) 41–46.
[48] N. Pangarov, On the crystal orientation of electrodeposited metals, Electrochim. Acta 9 (6) (1964) 721–726.
[49] R. Ke, C. Hu, M. Zhong, X. Wan, K. Wu, Grain refinement strengthening mechanism of an austenitic stainless steel: critically analyze the impacts of grain interior and grain boundary, J. Mater. Res. Technol. 17 (2022) 2999–3012.
[50] L. Lu, M. Sui, K. Lu, Superplastic extensibility of nanocrystalline copper at room temperature, Science 287 (5457) (2000) 1463–1466.
[51] Z. Cheng, T. Wan, L. Lu, Interface strain gradient enabled high strength and hardening in laminated nanotwinned Cu, Acta Mater. 256 (2023) 119138.
[52] F. Duan, Y. Naunheim, C. Schuh, Y. Li, Breakdown of the Hall-Petch relationship in extremely fine nanograined body-centered cubic Mo alloys, Acta Mater. 213 (2021) 116950.